RSC Advances

PAPER

View Article Online
View Journal | View Issue

Cite this: *RSC Adv.*, 2025, **15**, 44229

Synergistic effects of H_2O_2 on the performance of nano-zero-valent manganese biochar (nZVMn/PBC) for the treatment of chlorpyrifos from aqueous solution

Muhammad Aftab,[a] Zia Ul Haq Khan,*[a] Noor Samad Shah,[b] Maryam Zahid,[a] Jingyu Sun,[c] Mahmood M. S. Abdullah,[d] Fida Ullah[a] and Syed Khasim[e]

This study explores the efficient degradation of the highly toxic organophosphorus pesticide chlorpyrifos (CPY) from aqueous solution using a novel nano-zero-valent manganese-decorated plant biochar composite (nZVMn/PBC). The composite was synthesized *via* a chemical reduction method and thoroughly characterized using FTIR, XRD, SEM, TEM, EDS, XPS, and BET analyses. Characterization results revealed that nZVMn/PBC possessed a highly porous and crystalline structure enriched with abundant functional groups, favorable for catalytic degradation. Under optimized conditions ($[CPY]_0$ = 9 mg L^{-1}, $[nZVMn/PBC]_0$ = 25 mg L^{-1}, reaction time = 90 min), the composite achieved 84% degradation of CPY. Remarkably, the introduction of H_2O_2 further enhanced the degradation efficiency to 99% under identical conditions ($[H_2O_2]$ = 20 mg L^{-1}). The degradation was accelerated under basic pH and with increasing doses of H_2O_2 and nZVMn/PBC; however, excessive H_2O_2 concentrations reduced efficiency at higher pollutant levels. Mechanistic investigations revealed that hydroxyl radicals (•OH) were the dominant reactive species responsible for CPY decomposition. The nZVMn/PBC composite exhibited excellent stability and environmental compatibility. Analysis of the degradation intermediates confirmed the conversion of CPY into non-toxic products. Overall, this study demonstrates that the nZVMn/PBC–H_2O_2 system is a highly promising, sustainable, and efficient strategy for the degradation and detoxification of organophosphorus pesticides in contaminated water.

Received 8th September 2025
Accepted 23rd October 2025

DOI: 10.1039/d5ra06773a

rsc.li/rsc-advances

Introduction

Pesticides are synthetic substances used to inhibit, control, or eliminate unwanted species, such as pests of animals and fungi.[1] Based on the target organism, pesticides are categorized into various types, including herbicides, insecticides, fungicides, nematicides, acids, rodenticides, defoliants, and desiccants.[2,3] One of the most commonly used organophosphate insecticides globally is chlorpyrifos (CPY; $C_9H_{11}Cl_3NO_3PS$), synthesized by the Dow Chemical Company in 1965 as a household pesticide. It exhibits broad spectrum insecticidal efficacy against insect pests of commercial crops.[4,5] However, CPY poses significant threats to non-target organisms. In humans, CPY toxicity results in numerous clinical symptoms, including nervous system dysfunction, disruption of endocrine glands, and cardiovascular diseases affecting the heart, arteries, and veins.[6,7] National pesticide monitoring programs implemented in several countries have detected the presence of chlorpyrifos in food, soil, and water, raising concerns about its hazardous effects on consumers, farmers, and animals. Furthermore, CPY can alter the microbial population of a soil, including fungi, actinomycetes and bacteria, thereby inhibiting nitrogen mineralization. Chlorpyrifos exerts its toxic effect by inhibiting acetylcholinesterase activity. It is neurotoxic, genotoxic, and harmful to reproductive health.[5,8,9] CPY acts by inhibiting the critical enzyme acetylcholinesterase (AChE) in pests, disrupting their peripheral and central nervous systems. This mechanism similarly impacts the human nervous system, disrupting normal biochemical and physiological functions.[10] According to the WHO, 0.2 million people die and up to 2.5 million people suffer from acute pesticide poisoning globally each year.[11] Therefore, to mitigate the hazards posed to human health, prevent environmental contamination, and promote

[a]*Department of Chemistry, COMSATS University Islamabad Campus, Islamabad Park Road, Islamabad 45550, Pakistan. E-mail: ziaulhaqkhan11@gmail.com*

[b]*Department of Chemistry, COMSATS University Islamabad, Abbottabad Campus, 22060, Pakistan*

[c]*Hubei Key Laboratory of Pollutant Analysis & Reuse Technology, College of Chemistry and Chemical Engineering, Hubei Normal University, Cihu Road 11, Huangshan, Hubei 435002, PR China*

[d]*Surfactants Research Chair, Department of Chemistry, College of Science, King Saud University, P. O. Box 2455, Riyadh 11451, Saudi Arabia*

[e]*Advanced Materials Research Laboratory, Department of Physics, Faculty of Science, University of Tabuk, Tabuk 71491, Saudi Arabia*

sustainable farming practices, the degradation of pesticides such as chlorpyrifos is essential.[12] Consequently, various chemical and microbial techniques are employed to achieve their degradation. In recent years, the elimination of pesticides has relied increasingly on biological techniques and physico-chemical methods, such as advanced oxidation processes. However, these methods often result in incomplete breakdown of chlorpyrifos, producing byproducts that can be more hazardous than the parent compound.[13] One approach to improve this process involves the use of biochar, which resembles charcoal.[14] Biochar is environmentally friendly, exhibits exceptional porosity, and offers significant potential for environmental remediation.[13] As biomass is readily available, reusable, and cost-effective, its application for environmental cleanup is highly encouraged.[15,16] Additionally, its surface exhibits notable porosity and contains a high concentration of reactive functional groups, including alkyl, carboxyl (COOH), hydroxyl (OH), and aromatic groups. Biochar, in particular, is gaining popularity due to its ability to eliminate contaminants and activate peroxides to produce reactive oxygen species (ROS), such as the $^{\bullet}OH$ radical.[17–19] To achieve the desired physiological properties and catalytic efficiency, biochar derived from *Dracaena fragrans* stem was coated with nano-zero-valent manganese (nZVMn).[20] The unique advantage of the nZVMn composite biochar lies in its ability to combine the properties of a physical–biological–chemical (PBC) adsorbent, catalyst, and complex within a single material.[21] nZVMn, a prominent member of the group of zero-valent metals, is preferred to nano-zero-valent iron (nZVI) for pairing with PBC, due to its higher reduction potential of −1.18 V (ref. 22) compared to nZVI (−0.44 V).[23] Introducing zero-valent metal to the biochar surface increases the number of reactive sites. The small dimensions and enhanced photocatalytic capabilities of nano-zero-valent manganese further boost the potential of biochar for the catalyst-mediated degradation of chlorpyrifos.[24] The toxicity levels of chlorpyrifos are presented in Table 1.

Hydrogen peroxide (H_2O_2) is selected as the oxidative eliminator of chlorpyrifos due to its exceptionally high oxidizing potential of 2.8 V. It is used in combination with nZVMn/PBC. As indicated by reactions (1)–(3), the nZVMn on the surface of PBC oxidizes into manganese ions and facilitates the decomposition of hydrogen peroxide into hydroxyl radicals ($^{\bullet}OH$).

$$2Mn^0 + O_2 + 2H_2O \rightarrow 2Mn^{2+} + 4OH^- \quad (1)$$

$$Mn^0 + H_2O_2 \rightarrow Mn^{2+} + 2OH^- \quad (2)$$

$$Mn^{2+} + H_2O_2 \rightarrow Mn^{3+} + {}^{\bullet}OH + {}^{-}OH \quad (3)$$

As demonstrated by eqn (4) and (5), the evolved $^{\bullet}OH$ is a potent oxidant that reacts rapidly with organic pollutants at high rates, effectively breaking them down into degradation products (DPs):

$$^{\bullet}OH + CPY \rightarrow \text{intermediate} \quad (4)$$

$$^{\bullet}OH + CPY \rightarrow \text{intermediate} \rightarrow DPs \quad (5)$$

This research focused on synthesizing biochar using a stem extract of maize plants and evaluating its efficiency in adsorbing contaminants. PBC was combined with nZVMn to enhance its adsorption and recycling capacities while also functioning as a catalyst. Various advanced characterization techniques were employed to study the physiological properties of the synthesized nZVMn/PBC adsorbent. H_2O_2 was introduced in conjunction with nZVMn/PBC to facilitate the removal of chlorpyrifos. Through an adsorptive process, nZVMn/PBC effectively eliminated chlorpyrifos, and the underlying mechanisms were thoroughly investigated. Additionally, the effects of varying chlorpyrifos concentration, nZVMn dosage, and pH levels on removal efficiency were examined. The study also explored the potential for resource reuse and the catalyst-mediated conversion of H_2O_2 to $^{\bullet}OH$ *via* the solid-adsorbing compounds generated.

Characterization of PBC and nZVMn/PBC

To identify the functional groups and types of bonding present in plant-derived biochar (PBC) and synthesized nZVMn/PBC, an

Table 1 Toxicity of chlorpyrifos

Sr. no.	System	Concentration of CPY	Comments on toxicity	References
1	Human	300 μM	Blood cholinesterase activity affected	25
2	Zebrafish	300 μM	Inhibited AcHE & locomotor activity	26
3	Zebrafish	100–300 μg L^{-1}	Developmental toxicity, oxidative stress, neurotoxicity, locomotor activity	27
4	Mice lacking glutamate cysteine ligase	—	Oxidative stress & cytotoxicity	28
5	*Gasterosteus aculeatus*	1.75, 0.88, 0.35 0.12 μg	Lipopolysaccharides enhanced DNA damage	29
6	Japanese medaka (*Oryzias latipes*)	0.12 mg L^{-1}	Decrease in social behavior in 12 days	30
7	Rats	1 mg kg^{-1} (days 1–4)	Affected RNA concentrated & showed delayed neurotoxicity	26
8	Neonatal rats	1 mg kg^{-1} d^{-1}	Permanent changes in brain cells	31
9	Green algae	9.37–150 mg L^{-1}	Inhibited the growth & cell shape of cell organelles at high concentrations	32
10	Freshwater microalgae	0–100 mg L^{-1}	Inhibited the growth & content of chlorophyll at high concentration	32
11	Mice	0.28–8.96 mg kg^{-1}	DNA damage	33

FTIR spectrophotometer (Bruker, ISS-88) was used, operating in the range 400–4000 cm^{-1}. X-ray diffractometer analysis was employed to determine the phase composition, crystallinity, and homogeneity of the plant biochar and nano-zero-valent manganese-doped plant biochar. Scanning electron microscopy (SEM) (TESCAN-VEGA) was performed to analyze the surface morphology of the plant-derived carbonaceous material and hydrothermally synthesized nanocomposite (nZVMn/PBC). TEM (JEM-1011) at a resolution of 200 nm was used to examine the topographical features of the synthesized materials. SEM images were captured in second electron mode using a 5.0 V energy beam. The SEM images were further processed using ImageJ software to generate histograms of nanostructure diameters. An energy dispersive X-ray spectrometer (EDAX) (JED-2200 series) was used to determine the atomic ratio, atomic percentage and elemental composition of PBC and nZVMn/PBC. X-ray photoelectron spectroscopy (SPECSURF version 2.06), employing an Al Kα X-ray source (1486.6 eV, 6 mm beam size), was used to analyze the chemical composition and surface valence state of the materials. The adsorption efficiency of the PBC for pesticide removal was evaluated using ultraviolet-visible spectroscopy (OPTIZEN Alpha). The point of zero charge (pH_{pzc}) was calculated to determine the surface charge properties of Mn-doped PBC and nZVMn/PBC, while zeta potential (ZP) analysis was conducted to evaluate the stability of the synthesized bimetallic adsorbent material. BET analysis was carried out to determine the pore size, pore volume and surface area.

Materials and methods

Materials

All chemicals used in this study were of analytical grade and supplied by Sigma-Aldrich (now MilliporeSigma). These include chlorpyrifos (CPY), plant biochar (PBC), sodium borohydride ($NaBH_4$), hydrogen peroxide (H_2O_2), manganese(II) tetrahydrate ($MnCl_2 \cdot 4H_2O$), and ethanol. The high-purity water used in the reaction mixtures was produced using Millipore's Milli-Q® technology.

Preparation of corn-plant-derived biochar

Maize plants were used in this study to produce biochar. The plants were collected and thoroughly washed with distilled water to remove any dirt or contaminants. Subsequently, the maize plants were separated into parts and air-dried. The samples were further dried at 60 °C to eliminate residual moisture.[34] The dried stems were then ground into powder. 10 g of the powdered material was weighed and subjected to pyrolysis at 550 °C for 3 h in a high-temperature furnace. The pyrolysis process yielded biochar, which was used in subsequent experiments.[35]

Preparation of nZVMn/PBC composite

To synthesize the nZVMn/PBC composite, 1.0 g of $MnCl_2 \cdot 4H_2O$ and 0.5 g of PBC were dissolved in beakers containing 35 mL of distilled water and 5 mL of ethanol. Ethanol was used to minimize the oxidation of nZVMn during the preparation process. Separately, 1.0 g of sodium borohydride was dissolved in 40 mL of distilled water, and this solution was transferred to a burette. The BH_4^- solution was added dropwise to the beaker containing the $MnCl_2 \cdot 4H_2O$ and PBC suspension.[34] This gradual addition was carefully monitored to optimize the production of the nZVMn/PBC composite. The reaction mixture was sonicated, and the aqueous layer was removed to isolate the resulting products. The mixture was then oven-dried at 90 °C for 24 h. Finally, the dried nZVMn/PBC mixture was powdered and subjected to pyrolysis under limited oxygen conditions to produce the nZVMn/BC composite.[16,34]

Batch experiment and adsorption studies

To investigate the adsorptive elimination of CPF using synthesized materials, two independent pathways were examined. For the adsorption study, 1000 mg L^{-1} of plant biochar and nano-zero-valent manganese were added to a 300 mL Pyrex glass beaker containing an aqueous solution of CPY at a concentration of 30 mg L^{-1}. The mixture was studied over varying durations, ranging from 0 to 120 min. The pH of the pesticide solution was adjusted using NaOH and HCl across different pH values. Eqn (6) and (7) were used to predict the pesticide adsorption capability at equilibrium (q_e, mg g^{-1}) and at a specific time t (q_t, mg g^{-1}).[16]

$$q_e = \left(\frac{C_i - C_f}{M_a}\right) \times V_w \quad (6)$$

$$q_t = \left(\frac{C_i - C_t}{M_a}\right) \times V_w \quad (7)$$

In eqn (7), the variables C_i, C_f, and C_t denote the dye concentrations at start, final, and specific times (mg L^{-1}), V_w denotes the volume of solution (L), and M_a is the mass of the adsorbent (g).

Adsorption kinetics and mechanism

The pseudo-first-order and pseudo-second-order kinetics of nZVMn onto PBC were studied to understand the reaction process and identify the rate-controlling phase. At agitation time t, the amount of CPY adsorbed, q_t, is determined using the expression:

$$q_t = \frac{(C_o - C_t) \times V}{W} \quad (8)$$

The liquid-phase concentration of nZVMn/PBC solution, representing the adsorbate, is denoted as C_o at time t and C_t at any given time t. V_w remains consistent with its definition in eqn (6) and (7). The rate-determining step and adsorption mechanisms were analyzed by applying kinetic models to the experimental data obtained from optimization of the contact time.

The pseudo-first-order equation

The pseudo-first-order Lagergren equation describes the relationship between a solid and a liquid system based on the sorption capacity of nZVMn. One nZVMn ion is adsorbed onto a single PBC adsorption site.

$$\mathrm{nZVMn} + \mathrm{PBC} \xrightarrow{k_1} (\mathrm{nZVMn})\mathrm{PBC}_{(\text{sloid-phase})} \quad (9)$$

A pseudo-first-order mathematical form is typically written as:

$$\log(q_e - q_t) = \log\left(q_e - \frac{k_1 t}{2.303}\right) \quad (9a)$$

$$h_1 = k_1 q_e \quad (9b)$$

where q_t is the relative amount of nZVMn deposited at any given time interval (mg g^{-1}), q_e is the total amount of nZVMn adsorbed at equilibrium per unit weight of the adsorbent (mg g^{-1}), h_1 is the pseudo-first-order starting adsorption rate, k_1 is the pseudo-first-order rate constant (min^{-1}), $\log(q_e - q_t)$ should plot linearly with t and with k_1, q_e can be found by calculating the slope and intercept of the expression in eqn (9a).[36]

Pseudo-second-order equation

The chemisorption kinetics of the liquid system were examined using the pseudo-second-order rate expression. Furthermore, based on the interaction between nanoscale-zero-valent manganese (Mn) and PBC, it is proposed that Mn is adsorbed onto adsorption sites on the PBC surface.

$$2\mathrm{nZVMn} + \mathrm{PBC} \xrightarrow{k_2} (\mathrm{nZVMn})_2\mathrm{PBC}_{(\text{sloid-phase})} \quad (10)$$

The linear form of a pseudo-first-order equation is typically written as follows:

$$\frac{1}{q_t} = \frac{1}{k_2 {q_e}^2} + \frac{1}{q_e} t \quad (10a)$$

When t tends to zero, h_2 is defined as:

$$h_2 = k_2 {q_e}^2 \quad (10b)$$

Substituting the value of h_2 into the above equation, it becomes:

$$\frac{1}{q_t} = \frac{1}{h_2} + \frac{1}{q_e} t \quad (10c)$$

where h_2 represents the initial rate of adsorption. If the second-order kinetic equation is applicable, plotting t/q_t against t should yield a linear relationship. From this plot, constant k_2, q_e and h_2 can be determined.[36]

Adsorption isotherm models

The amount of material adsorbed per unit mass of the adsorbent is related to the equilibrium concentration of the material at a constant temperature by an adsorption isotherm.

Freundlich isotherm model

An equation describing both the surface variation and the exponential pattern of reactive sites and their energy is provided by the Freundlich adsorption isotherm. The linear form of the Freundlich equation is:

$$\log Q_e = \log k_f + \frac{1}{n} \log C_e \quad (11)$$

The parameters defining the adsorbent–adsorbate system are the Freundlich isotherm constants, k_f and n_f, which represent the adsorption capacity and intensity, respectively. These constants are determined from the slope and intercept of a plot of $\log Q_e$ *vs.* $\log C_e$.

Langmuir isotherm model

The Langmuir adsorption isotherm is assumed to apply when single-layer adsorption occurs on a homogeneous surface with a finite number of identical adsorption sites. During adsorption, no migration of adsorbed molecules takes place on the surface, which maintains a constant adsorption energy. The linear expression for the Langmuir isotherm is:

$$\frac{C_e}{Q_c} = \frac{1}{K_L Q_{max}} + \frac{C_e}{Q_{max}} \quad (12)$$

The maximal monolayer coverage capacity is expressed as Q_{max} (mg g^{-1}). The Langmuir isotherm constant, or K_L (mg^{-1}), represents the adsorption energy. The equilibrium parameter, also known as the separation factor, is a dimensionless constant that reflects the main characteristics of the Langmuir isotherm and can be derived from it.

$$R_L = \frac{1}{1 + K_L C_o} \quad (13)$$

The adsorption nature is indicated by the R_L value, which can be either favorable or unfavorable.

Results and discussion

Characterization of PBC and nZVMn/PBC

The synthesized plant biochar and nano-zero-valent manganese-doped plant biochar were analyzed for physical, crystallographic, and surface characteristics using various advanced techniques, including FTIR, XRD, SEM, EDS, XPS, and TEM.

FTIR interpretation. The FTIR spectra of the synthesized nano-zero-valent manganese/plant biochar in the wavenumber range from 4000 to 550 cm^{-1} are shown in Fig. 1. The FTIR spectra of PBC were published in our previous paper.[37] They exhibit distinctive vibrations at 3437, 2922, 2027, 1626, 1335, 1004 and 670 cm^{-1}. A large and broad spectral peak at 3437 cm^{-1} is associated with adsorbed water O–H stretching.[38] Potential causes of the peaks at 2922 cm^{-1} could be the –C–H stretching vibration of the newly created materials. The faint peaks at 2080 cm^{-1} could be explained by the existence of –C=C=C– bonds. The peak at 1626 cm^{-1} justifies the presence of coupled C=C stretching in the solid material. In addition, vibrations of the produced materials at 1337 cm^{-1} and

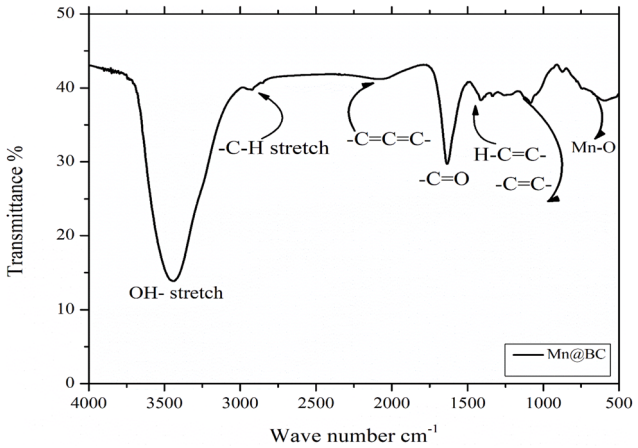

Fig. 1 FTIR spectra of the synthesized nZVMn/BC materials.

1004 cm^{-1} were detected in the spectra, which revealed the existence of H–C═C– and –C═C– groups. In accordance with the existence of an Mn–O bond, the nano-zero-valent manganese-doped plant biochar displayed a peak at 670 cm^{-1}, indicating that Mn had been successfully coupled with the biochar.[22,36] The effectiveness of biochar is said to be significantly influenced by the existence of aromatic structure, carbon concentration, and –OH groups.[38,39]

X-ray diffraction analysis. X-ray diffraction analysis nZVMn/PBC XRD provided valuable insights into the present phase, crystallographic structures, and composition. The XRD spectrum of PBC was published in our previous paper.[37] XRD analysis of nZVMn/PBC showed diffraction peaks at 14.88°, 25.95°, 31.96°, 33.56°, 41.55°, 42.86°, 45.71°, 51.52°, and 56.78°, corresponding to the lattice planes (222), (200), (110), (11), (11), (01), (010), (002) and (100), respectively. For nZVMn/PBC, the XRD pattern revealed peaks at $2\theta = 25.95°$, 31.96°, 33.56°, and 51.52°, which are attributed to the amorphous form of MnO_2. Additionally, strong and intense peaks were observed for Mn_2O_3 at $2\theta = 14.88°$ and 56.78°. The peaks observed at $2\theta = 41.55°$, 42.86°, and 45.71° correspond to Mn^0 (Fig. 2). The zero-valent manganese substance is identified by distinctive peaks in the

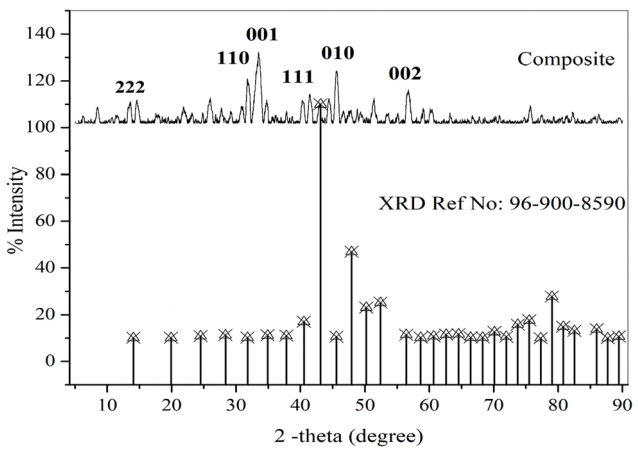

Fig. 2 XRD spectrum of nZVMn.

nZVMn/PBC. Using the Debye–Scherrer equation, the average crystallite size of the material was calculated from the peak at 45.71° (001) in the XRD graph, and was found to be 33.38 nm.[40]

Scanning electron microscopy. SEM analysis of the biochar displayed a highly porous structure linked to its composition (Fig. S1).[16] Additionally, SEM was also utilized to analyze the morphology of the nanomaterials.[41] SEM micrographs of the synthesized nZVMn/PBC materials revealed their morphological and structural properties (Fig. 3A–C). High-quality SEM images of randomly selected particles were used for observation, with average particle size and size distribution histograms generated (Fig. S2). In the case of nZVMn/BC, the nZVMn nanoparticles were evenly distributed across the outermost PBC layer. Moreover, the nZVMn/BC composite exhibited a porous exterior, offering numerous active adsorption sites that facilitate the capture of relevant contaminants.[16] EDS analysis was performed to identify elemental composition. For nZVMn/PBC, EDS analysis detected Mn as a prominent and sharp peak, alongside C and O (Fig. 3D). The Mn peak in the nZVMn/PBC composite further confirmed the successful integration of nZVMn into the biochar. Additionally, the EDS spectra of nZVMn/PBC showed peaks corresponding to chlorine (Cl), silicon (Si) and sodium (Na), attributed to the precursor manganese salt (manganese(II) chloride tetrahydrate) and sodium borohydride. Table 2 shows the elemental analysis of nZVMn/PBC.

Transmission electron microscopy. The TEM image of the prepared nZVMn/PBC is shown in Fig. S3. TEM analysis revealed that the nZVMn/PBC surface is highly crystalline, oval-shaped, homogeneous, consistent and nanoscale. As can be observed in the figure, the Mn^0 nanoparticles exhibit an oval morphology and are predominantly single-crystalline.[41] The effective catalytic efficiency in the degradation mechanism depends significantly on the crystalline nature of the synthesized material.[42]

X-ray photoelectron spectroscopy. The elemental composition, chemical state, and electronic state of the material were investigated using XPS. XPS analysis identified Mn, C, and O as the primary components of nZVMn/PBC. The XPS analysis, as shown in Fig. 4, showed the presence of Mn^0 in nZVMn/PBC, confirming that the borohydride-based chemical reduction process successfully synthesized Mn^0. The results indicate that zero-valent manganese (Mn^0) exhibited a binding energy of 639.6 eV for Mn $2p_{3/2}$. The charge transition from Mn^0 to Mn^{4+} results in binding energies of 640.6 eV (Mn $2p_{3/2}$) for Mn^{2+}, 641.3 eV for Mn^{3+} and 642 eV for Mn^{4+}.[43,44] The oxidation states of $Mn2p_{1/2}$ appear at 252 and 254 eV, respectively. The O 1s spectra revealed a single component at 530.4 eV, which was further deconvoluted into three peaks, corresponding to the Mn–O lattice, Mn–OH and adsorbed water molecules on the surface of the photocatalyst. The carbon spectrum shows the presence of C–C, C–OH and C–O.

Brunauer–Emmett–Teller (BET) analysis

The synthesized biochar doped with nano-zero-valent manganese (nZVMn) was analyzed for its BET surface area and pore

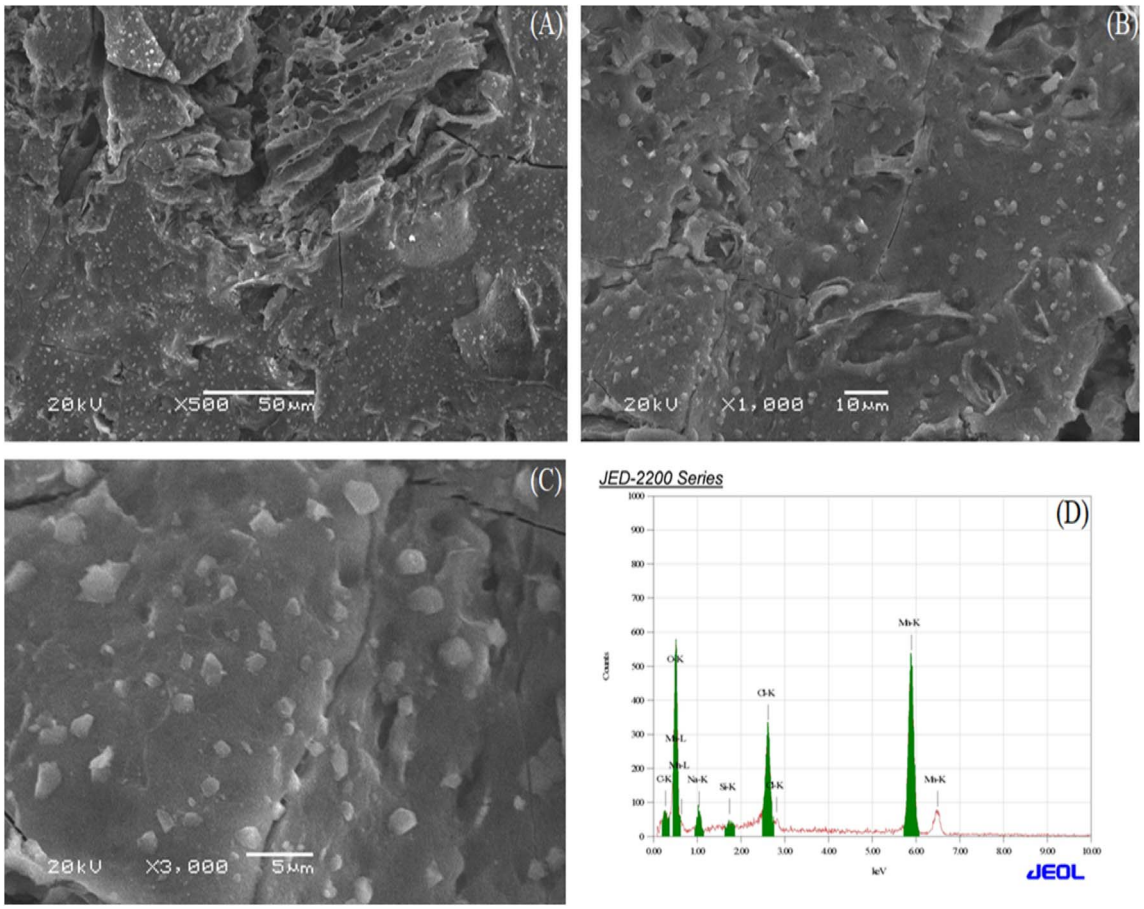

Fig. 3 SEM (A), (B), (C), and EDS (D) images of synthesized nZVMn/PBC.

Table 2 Elemental analysis of nZVMn/PBC

Element	keV	Mass%	Atomic%	Error%
C	0.277	7.78	17.10	0.35
O	0.525	28.98	47.83	0.25
Na	1.041	3.76	4.32	0.43
Si	1.739	0.31	0.29	0.23
Cl	2.621	7.69	5.72	0.17
Mn	5.894	51.48	24.74	0.56
Total		100%		100%

size using N_2 adsorption–desorption studies conducted at 77 K. The nZVMn/PBC composite exhibited a mesoporous morphology with irregular pores. The adsorption isotherm displays type IV features and an H_3 hysteresis loop. The analysis revealed that the nZVMn/PBC composite had a BET surface area of 27.0630 $m^2\ g^{-1}$, pore volume of 0.169669 $cm^3\ g^{-1}$, and average pore size of 292.7 Å, as shown in Fig. 5. For comparison, the BET analysis of PBC is presented in SI Fig. S4. Compared to the BET of PBC, the nZVMn/PBC composite exhibits significantly higher surface area and pore volume, indicating that the incorporation of nZVMn substantially enhanced the porosity of the material, suggesting that nZVMn plays a crucial role in enhancing the structural characteristics of the biochar. The results underscore the potential of nZVMn/PBC as an advanced material with improved porosity and surface properties.[45,46]

Point of zero charge

The pH at which the net charge on a material surface is zero is referred to as the point of zero charge (pH_{pzc}). This parameter is critical for understanding electrostatic interactions between solid-adsorbent materials and surrounding solutions. When the solution pH is higher than pH_{pzc} ($pH > pH_{pzc}$), the surface of the adsorbent material typically carries a net negative charge due to deprotonation and increased concentration of hydroxyl ($-OH^-$) ions. This condition favors the adsorption of cationic species. Conversely, when the solution pH is lower than pH_{pzc} ($pH < pH_{pzc}$), the surface acquires a net positive charge due to protonation and the prevalence of hydrogen ions (H^+), which enhances the adsorption of anionic species.[47] The calculated pH_{pzc} value for nZVMn/PBC, determined by the point of intersection method, is 7.5 (Fig. S5). This indicates that the surface of the photocatalyst is anionic above pH = 7.5 and cationic below this value. Zeta potentials (ZP) with a ZP value close to ±10 mV are considered neutral, while those with a ZP value of <−30 mV or >+30 mV are regarded as strongly anionic and cationic, respectively.[48] ZP measurements are also indicative of nanoparticle stability; particles with ZP values near ±10 mV

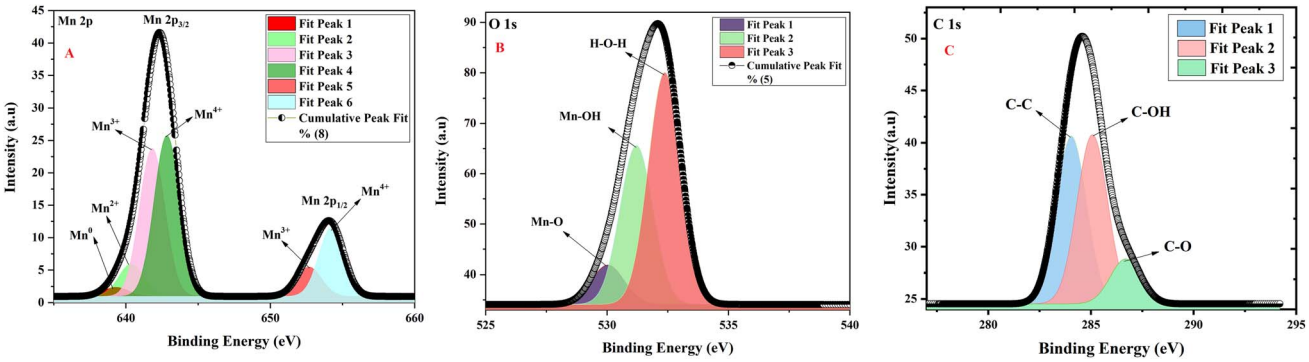

Fig. 4 XPS spectra: Mn 2p (A), O1s (B), C 1s (C).

exhibit minimal stability and are prone to agglomeration, whereas higher ZP magnitudes suggest greater stability. For the synthesized nZVMn/PBC material, the measured ZP is 35.34 mV, which confirms excellent stability and a strong anionic surface, consistent with pH_{pzc} (Fig. S6). These properties make nZVMn/PBC highly suitable for the degradation of pesticides.

Band gap

Manganese oxide (MnO) is a transition metal oxide with a narrow band gap, typically ranging from 3.6 to 4.2 eV, depending on its crystal phase, particle size, and synthesis method.[49] The band gap represents the energy difference between the valence band (occupied by electrons) and the conduction band (where electrons can move freely). In MnO, this band gap allows it to absorb light mainly in the ultraviolet region, although modification or doping can extend its absorption into the visible region.[50] The photocatalytic activity of MnO arises from its semiconducting nature.[51] When exposed to light with energy equal to or greater than its band gap, electrons are excited from the valence band to the conduction band, leaving behind holes. These photogenerated electron–

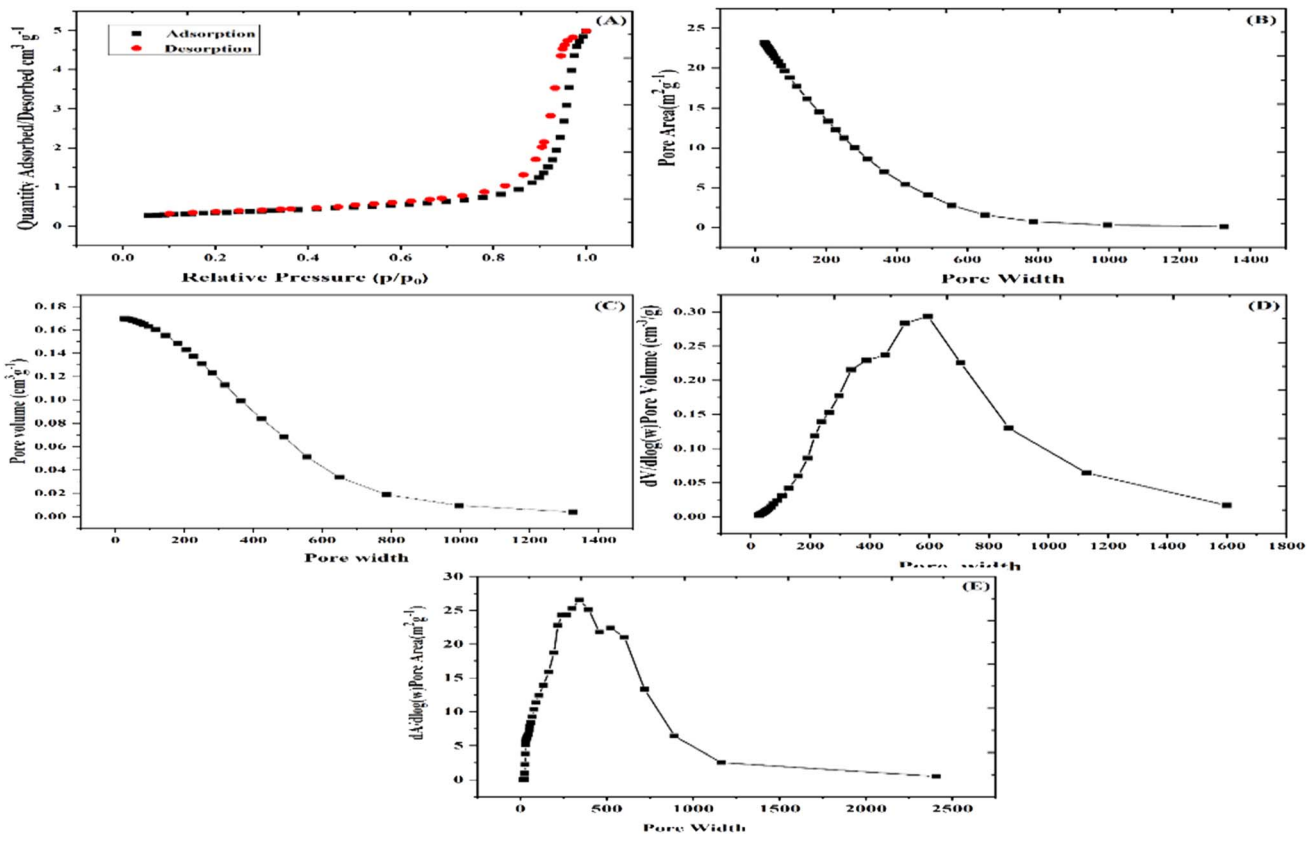

Fig. 5 (A) BET Adsorption–desorption isotherm of synthesized nZVMn/PBC (B–E) enlarged overview of pore width, pore volume and pore size.

hole pairs participate in redox reactions—electrons reduce molecular oxygen to form superoxide radicals ($O_2^{\bullet-}$), while holes oxidize water or organic pollutants to produce hydroxyl radicals ($^{\bullet}OH$). These reactive oxygen species (ROS) are responsible for degrading organic contaminants and promoting antibacterial or environmental purification processes. Furthermore, the narrow band gap and multiple oxidation states of Mn (Mn^{2+}, Mn^{3+}, Mn^{4+}) enhance charge separation and facilitate efficient electron transfer, improving the overall photocatalytic performance. MnO-based materials are therefore promising candidates for photocatalytic degradation of dyes, wastewater treatment, and energy conversion applications.[52] The band gap of nZVMn@BC is presented in Fig. S7.

Impact of various parameters on the degradation of chlorpyrifos

A variety of process factors, including CPY concentration, pH, light conditions, and acidic and basic environments, were evaluated for their influence on CPY degradation using nZVMn/PBC-catalyzed H_2O_2.

Effects of various light exposures, acidic and basic conditions

Numerous experiments were conducted to investigate the degradation of chlorpyrifos solution. Fig. 6 displays the effects of various conditions, including controlled (dark) conditions, exposure to visible light, UV light, and basic and acidic conditions, on the degradation process. Under controlled conditions in a dark environment employing a catalyst, minimal degradation was observed. This indicated that the catalyst exhibits significantly higher activity in the presence of light compared to darkness. To further explore the impact of light exposure, multiple experiments were performed to assess the photodegradation of CPY under different light sources. As shown in Fig. 6, visible and UV light were evaluated for their effects on CPY degradation. The results revealed a marked difference in degradation efficiency between the light sources, depicting a low degradation efficiency of 6% under visible light compared to 8% under UV light. The short wavelength and high energy of UV light are particularly effective for initiating photodegradation.[53] Experiments were also conducted under acidic and basic conditions. The degradation of CPY was higher under basic conditions (12%) than under acidic conditions (10%), as shown in Fig. 6A. Chlorpyrifos contains a phosphorus atom, which is susceptible to hydrolysis, a process where a water molecule breaks down chemical bonds. In basic conditions, hydrolysis occurs more readily because hydroxide radicals ($^{\bullet}OH$) are abundant, facilitating the breakdown of phosphorus compounds.[11] In acidic conditions, the concentration of H^+ is higher, and hydrolysis is less favorable because there are fewer hydroxide radicals ($^{\bullet}OH$) available to react with chlorpyrifos. Therefore, chlorpyrifos is less likely to undergo degradation in an acidic environment than in a basic one.[54]

Adsorption of CPY pesticide by PBC and nZVMn/PBC

In order to eliminate the pesticide CPY from water, an adsorption experiment was carried out. 100 mL of an aqueous solution of CPY from a stock solution containing 20 mg L^{-1} received treatment with 1000 mg L^{-1} of plant biochar and nano-zerovalent manganese/plant biochar nanocomposite material with pH = 8, adjusted by H_2SO_4 (0.5 M) and NaOH (0.5 M) solutions, respectively. After 90 min of reaction time, PBC exhibited 48% adsorption for CPY, whereas the nZVMn/PBC adsorbent material exhibited 90% adsorption, as displayed in Fig. 6B.

Effects of CPY concentration

nZVMn/PBC-catalyzed H_2O_2-based degradation was carried out under different CPY dosages (3, 6, 9 and 12 mg L^{-1}) at constant nZVMn/PBC concentration and constant initial pH (pH = 8.0). The results were 80% and 99% at higher concentration and lower concentration of CPY, respectively (Fig. 7A). These findings imply

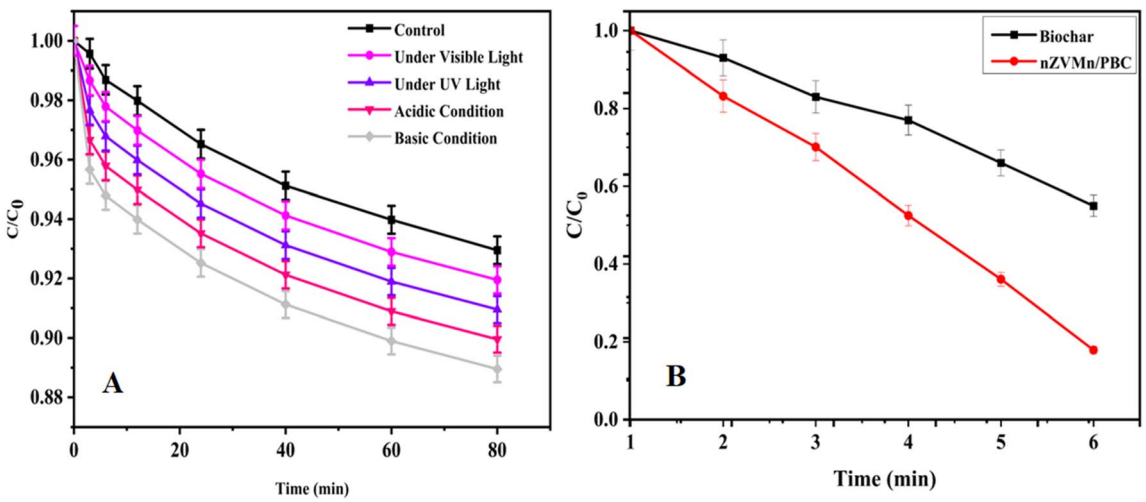

Fig. 6 (A) Effect of various light exposure, acidic and basic conditions on degradation of CPY [experimental conditions: CPY = 1000 mg L^{-1}, pH = 8.0]. (B) Adsorption of CPY by biochar and nZVMn/PBC [experimental conditions: UV light, $[nZVMn/PBC]_0$ = 1000 mg L^{-1}, $[CPY]_0$ = 100 mg L^{-1}, $[H_2O_2]_0$ = 10 mg L^{-1}, temp. = 25 °C, 30 °C, and 35 °C, pH = 8.0, reaction time 20–120 min].

that there is an inverse relationship between CPY concentration and CPY degradation efficiency. The outcomes attained align with those already reported in literature.[55–57] The potential for a reduction in the concentration of ˙OH radicals at a higher level of CPY concentration, as opposed to lower levels, could contribute to an elevation in the formation of DPs and hinder the penetration of light within the water solution. Additionally, the anticipated outcome leading to a decrease in degradation efficiency might arise from intensified competition between CPY and its degradation products (DPs) at high contamination concentrations, preventing their accumulation on the surface of the synthetic material[58,59]

Effect of nZVMn/PBC concentration

The elimination of CPF was studied under conditions of a fixed concentration of CPY = 100 mg L^{-1} and a constant pH = 8.0, utilizing varying quantities of the plant biochar material and solid-adsorbent material nano-zero-valent manganese: 5, 10, 15, 20 and 25 mg L^{-1}. The findings revealed a notably higher efficiency in CPY removal at a higher dosage of the synthesized adsorbent material compared to a lower dosage. By increasing the adsorbent concentration from 5 to 25 mg L^{-1}, degradation efficiency increased from 30% to 84% (Fig. 7B). This trend was consistent with previous studies.[60–62] By increasing the dosage of the nanocomposite, the amount of available active binding sites increased, consequently facilitating the binding of a substantial number of target contaminant molecules. Conversely, at lower dosages, the availability of active binding sites decreases, resulting in a lower capacity to capture contaminant molecules.[63] Additionally, the aggregation of synthesized adsorbent material intensifies at higher concentrations of synthesized adsorbent material, while it diminishes with lower doses, following the opposite pattern.[63]

Effects of pH

CPY degradation by nZVMn/PBC-catalyzed H_2O_2 was assessed using a variety of aqueous solutions with a range of pH values (3.0–11.0). The change in pH has an enormous impact on the photocatalytic degradation of CPY. Maximum degradation of CPY was observed at pH 8.0, while lower degradation was observed at pH 3.0 and 11.0. The ionic strength of the target contaminant and the propensity for oxidation of reactive radicals, and surface charge of the photocatalyst are all said to be

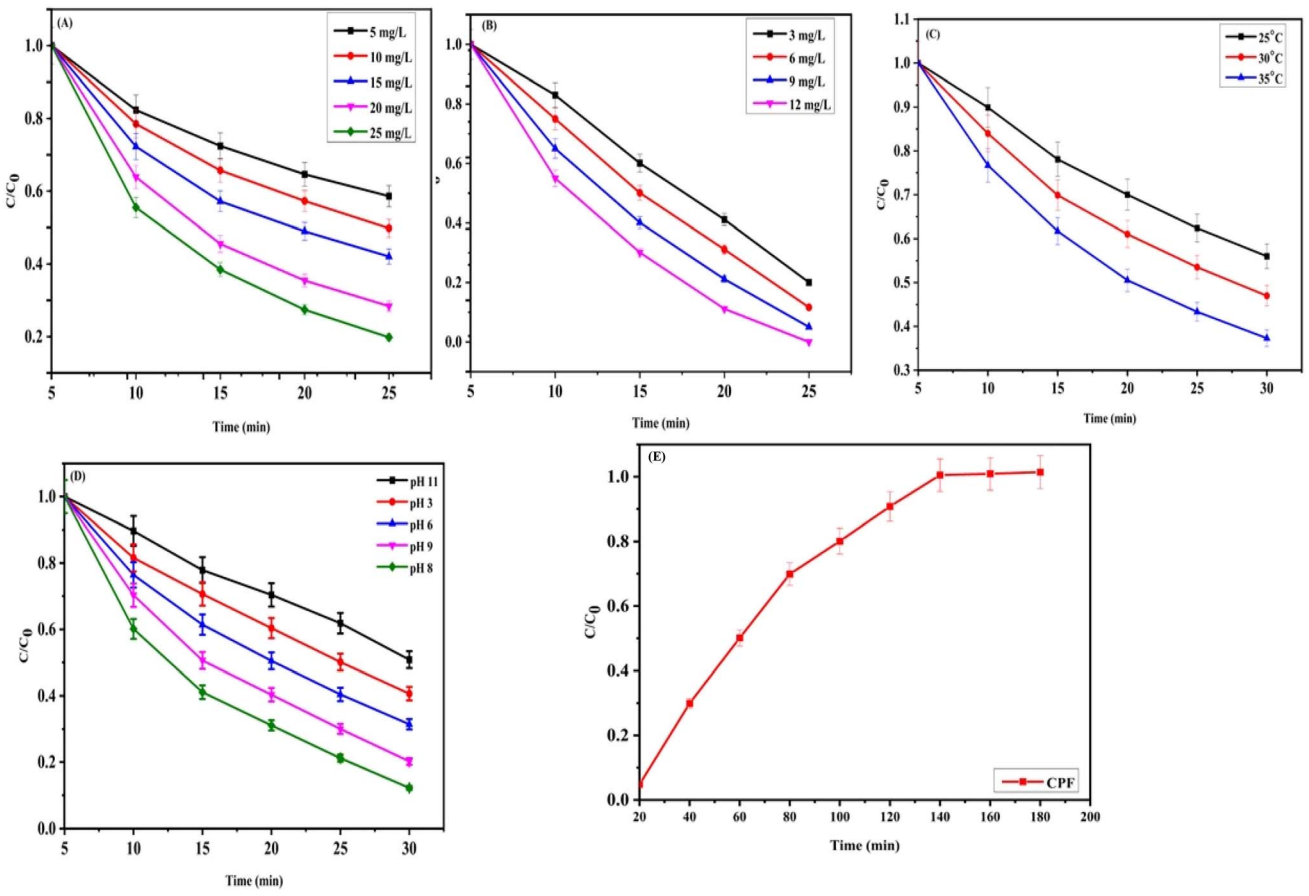

Fig. 7 (A) Effects of CPY concentration [experimental conditions: UV light, $[nZVMn/PBC]_0 = 1000$ mg L^{-1}, $[CPY]_0 = 3$, 6, 9 and 12 mg L^{-1}, pH = 8.0]. (B) Effect of nZVMn/PBC dosage [experimental conditions: UV light, $[nZVMn/PBC]_0 = 5$, 10, 15, 20, and 25 mg L^{-1}, $[CPY]_0 = 100$ mg L^{-1}, pH = 8.0]. (C) Effect of temperature [experimental conditions: UV light, $[nZVMn/PBC]_0 = 1000$ mg L^{-1}, $[CPY]_0 = 100$ mgL^{-1}, $[H_2O_2]_0 = 10$ mg L^{-1}, temp = 25 °C, 30 °C, and 35 °C, pH = 8.0]. (D) Effects of pH [experimental conditions: UV light, $[nZVMn/PBC]_0 = 1000$ mg L^{-1}, $[CPY]_0 = 100$ mg L^{-1}, pH = 3.0, 6.0, 9.0, 8.0, and 11.0]. (E) Impact of contact time [experimental conditions: UV light, $[nZVMn/PBC]_0 = 1000$ mg L^{-1}, $[CPY]_0 = 100$ mg L^{-1}, $[H_2O_2]_0 = 10$ mg L^{-1}, temp. = 25 °C, contact time 20–120 min, pH = 8.0].

impacted by changes in pH.[64–66] The increased deprotonation of nanoparticles at higher pH levels enhanced the removal efficiency from 40% to 65%, as the resulting negatively charged photocatalyst surface promoted greater chlorpyrifos adsorption.[67,68] The calculated value of the point of zero charge (pH_{pzc}) for nZVMn/PBC according to the point of intersection was 7.5 (Fig. 7D), indicating that the photocatalyst surface is anionic above this pH and cationic below it.[44,69] Considering the pK_a value of chlorpyrifos of 4.84, this suggests that the compound carries a negative charge at pH greater than 4.83 and a positive charge at pH less than 4.83. Interaction between pollutant and photocatalyst, as well as the efficiency of photodegradation, is influenced by the combined effect of working pH, pH_{pzc} and pK_a of the pollutant. The lower percentage degradation of chlorpyrifos at pH < 6.0 and pH > 8.0 can be attributed to repulsion between nZVMn/PBC and chlorpyrifos because they have the same charges. Other potential reasons include scavenging of hydroxyl radicals ($^{\bullet}OH$) at acidic pH and minimization of oxidation strength at high pH levels.[70,71]

Effect of temperature on the degradation of chlorpyrifos

At different temperatures, 25 to 35 °C, the impact on decomposition of chlorpyrifos was investigated, keeping other parameters constant: [CPY] = 100 mg L^{-1}, [nZVMn/PBC] = 1000 mg L^{-1}, reaction time = 90 min and pH = 8 for chlorpyrifos. As the temperature increased, the degradation efficiency of nZVMn/PBC also increased, resulting in higher degradation of chlorpyrifos, such as 40% at 25 °C, 50% at 30 °C and 30% at 35 °C (Fig. 7C). According to temperature-based research, chlorpyrifos readily degrades as the temperature rises. This might result from stimulation of the solvent molecules, which would provide more heat energy and cause the chlorpyrifos structure to disintegrate. Temperature changes also affect the stability of both chlorpyrifos and the nZVMn/PBC catalyst. Elevated temperature destabilizes chlorpyrifos molecules, making them more prone to degradation. The findings presented in our study closely resemble those found in ref. 72.

Impact of contact time on degradation of CPY

One of the fundamental parameters used to maximize uptake and illustrate the kinetics of the adsorption process is contact time. To maximize the possibility of contact between the adsorbent and adsorbate, the duration of reaction time is increased. Adsorption tests were conducted with different reaction times, varying from 20 to 120 minutes, while maintaining other parameters constant: pH = 8.0 for CPY, [pesticide] = 5 mg L^{-1}, and nano-zero-valent manganese/plant biochar = 1000 mg L^{-1}. The results are displayed in Fig. 7E. The initial high adsorption rate is due to the fast adhesion of CPY on the nZVMn/PBC surface for 120 minutes. According to recent experiments, the chlorpyrifos (CPF) insecticide reached adsorption equilibrium in 120 minutes. The key to fast adsorption by nZVMn/PBC was the substantial number of available unoccupied active sites, which the pesticide molecules gradually filled over a time of 120 minutes. After that, the pesticide adsorption process stabilized, possibly as a result of saturation of active sites or due to the electrostatic repulsion among the pesticide molecules that had already been adsorbed.[73] When creating a cost-effective adsorbent for the treatment of contaminated water, one of the parameters considered is the minimum equilibrium time. Because of this, the exceptional CPY adsorption by the synthesized nZVMn/PBC material is possible.

Adsorption and kinetic modeling

The kinetic and equilibrium experimental adsorption data for the pesticide were confirmed using kinetic models (pseudo-first-order and pseudo-second-order) and equilibrium models (Langmuir and Freundlich). The fitting behavior of these models for the adsorption of pesticide onto nZVMn/PBC is illustrated in Fig. S8, and the corresponding model parameters are illustrated in Table 3. The maximum adsorption capacity (q_{max}) for CPY onto nZVMn/PBC was determined to be 0.27 mg g^{-1}. The Freundlich model exhibited a superior fit compared to the Langmuir model for chlorpyrifos with an R^2 value $\geq$ 0.98. For kinetic modeling, the pseudo-first-order kinetic model provided a better fit than the pseudo-second-order kinetic model, as indicated by an R^2 value of $\geq$0.807. The Freundlich model fit suggested the presence of potential multilayer adsorption and a heterogeneous adsorbent surface with a varying site affinity. The pseudo-first-order kinetic fit asserted that physical adsorption mechanisms control the adsorption process, where the rate is influenced by the number of available sites.

Reusability of biochar and nZVMn/PBC

The potential and long-term effectiveness of synthesized solid plant biochar and nano-zero-valent manganese/plant biochar materials were examined by assessing their performance in treating CPY over seven consecutive cycles, with the addition of H_2O_2. The findings demonstrated that, for five cycles in a row, both prepared materials consistently removed CPY; however, at the seventh cycle, the effectiveness of PBC dropped and resulted in 22% removal of CPY. Conversely, nZVMn/PBC demonstrated robust performance even at seven cycles, removing 40% of the CPY (Fig. S9). The outcomes demonstrated 78% and 60% decreases in CPY elimination over 7 cycles using plant biochar and nZVMn/PBC, respectively. A factor with scientific significance is that the magnetic properties of nZVMn improve the healing of the solid-adsorbent composite at the conclusion of the investigation. The stability and durability of the prepared nZVMn were boosted by the composite containing biochar, ethanol, and saturated N_2 gas. This improved the ability of the newly created nZVMn/PBC to remove CPY until the seventh cycle.

Comparative analysis of the degradation of chlorpyrifos using different metal composites and nZVMn/PBC

Degradation efficiency can only be maximized by determining the ideal photocatalysis conditions. Table 4 lists the most recent research on the photodegradation of several kinds of pesticides by metal oxide nanoparticles and their composites when

Table 3 Parameters of equilibrium and kinetic adsorption models for the modeling of pesticide adsorption by nZVMn/PBC nanocomposite

Type	Model name	Parameter	Chlorpyrifos
Equilibrium adsorption models	Langmuir	K_L (L mg^{-1})	0.590
		q_{max} (mg g^{-1})	0.27
		R^2	0.94
	Freundlich	K_F ([mg g^{-1} (L mg^{-1})$^{1/n}$])	2.39
		n	3.85
		R^2	0.98
Kinetic models	Pseudo-first-order	k_1 (min^{-1})	0.304
		q_e (mg g^{-1})	2.071
		R^2	0.807
	Pseudo-second-order	k_2 (g mg^{-1} min^{-1})	0.0005
		q_e (mg g^{-1})	7.675
		R^2	0.240

exposed to UV or visible light. The circumstances that match the highest degradation efficiency found in the studies have been published. The nZVMn/PBC composite offers significant advances over conventional environmental remediation materials. Both organic and inorganic contaminants can be effectively removed, due to their special blend of increased surface area, redox activity, sustainability, and multifunctionality. nZVMn particles offer a greater surface area per unit mass than conventional materials because of their nanoscale size. Even more porosity and surface area are displayed by the composite material when PBC (porous biochar) is added, owing to the enhanced adsorption capacity for contaminants.[16] The benefits of using biochar and manganese together for environmental cleanup rely heavily on the special redox characteristics of manganese (Mn). Manganese, in its zero-valent form, may remove harmful heavy metals like arsenic (As(v)) and chromium (Cr(vi)) and effectively break down organic contaminants like dyes, medication, and pesticides.[74] In comparison to more costly adsorbents or catalysts, such as activated carbon or other designed nanomaterials, porous biochar, which is frequently made from agricultural waste, is an economical and environmentally beneficial option. Because of its capacity to trap carbon, the manufacture of biochar also has a sustainable aspect, reducing its overall environmental impact.[75] nZVMn/PBC exhibits better stability than conventional nano-adsorbents because of the protective biochar matrix, which

Table 4 Comparative analysis of the degradation of chlorpyrifos using different metal composites and nZVMn/PBC

Adsorbent	Structure	Light source	Conc. of pesticide	Dosage of adsorbent	Contact time (min)	pH	Degradation efficiency (%)	References
CuO/TiO_2/PANL nanocomposite	Spherical NPs embedded in PANL	Visible	20 mg L^{-1}	5 mg	90	7.0	95	78
CeO_2/TiO_2/SiO_2 nanocatalyst	Nearly spherical	UV	2 mg L^{-1}	0.21	90	5.4	81.1	79
CeO_2–SiO_2 NPs	—	UV	10 mL aqueous sol	7 mg	150	9.0	90	80
Fe-doped CeO_2–SiO_2 nanocomposite	Spherical NPs	UV	20 mg L^{-1}	7 mg	230	9.0	81.31	81
S-doped Ni–Co nanocomposite	Dispersed spherical	Visible	2.5 mg L^{-1}	60 mg	150	10	92.5	81
GO–Fe_3O_4/TiO_2 nanocomposite	Mesoporous TiO_2 dispersed on GO nanosheets	Visible	5 mg L^{-1}	100 mg	60	8.0	97	82
ZnO/TiO_2–Fe_3O_4 nanocomposite	Fe_3O_4 uniformly distributed on porous nanostructure of ZnO	Visible	8 mg L^{-1}	60 mg	50	10	94.8	83
Cu–ZnO nanoparticles	Cu NPs embedded onto ZnO surface	Sunlight	200 mg L^{-1}	250 mg	240	6.0	91	84
ZnO@CdS nanostructures	CdS aggregated spherical NPs and ZnO nanoflowers	Sunlight	2 mg L^{-1}	25 mg	360	7.0	91	85
Fe–ZnO nanocomposite	Rough surface	UV	10 mg L^{-1}	25 mg	60	3.0	93.5	86
Ag–ZnO nanocomposite	Uniform distribution of Ag onto ZnO surface	Sunlight	50 mg L^{-1}	20 mg	40	3.0	90	87
Nano-zero-valent manganese-doped plant biochar	nZVMn uniformly distributed on the surface of PBC	UV	3 mg L^{-1}	20 mg	120	8.0	99	Present study

inhibits the oxidation of zero-valent manganese and lessens manganese leaching.[17] nZVMn/PBC can be modified for a number of environmental applications, such as the elimination of heavy metals and other inorganic pollutants or the redox-mediated breakdown of organic contaminants. Its versatility for application in various environmental contamination scenarios is enhanced by its multifunctionality, which also makes it preferable to single-purpose materials.[76] In comparison to other traditional materials, the degradation kinetics of pollutants are faster due to the high surface reactivity and electron-donating capability of nZVMn in the composite. Particularly in dynamic systems where rapid response times are crucial, this high reaction rate enhances the effectiveness of therapeutic procedures.[77]

Photocatalytic degradation of CPY

When the photocatalyst is exposed to UV or visible light with energy equivalent to or greater than the band gap, the process of photocatalytic degradation begins.[88] A schematic degradation pathway is shown in Fig. 8.

The nZVMn/PBC nanocomposite is said to release electrons, captured by CPY, a superior electron acceptor, which starts the degradation process. Upon exposure to visible light, e^-/h^+ pairs are produced as a result of the excitation of photo electrons from their valence band to their conduction band in MnO.[89] The breakdown of pesticides is caused by the extremely active hydroxyl radical (˙OH) that is created *via* an oxidation–reduction reaction (eqn (14)–(20)), when photogenerated e^-/h^+ are promoted to the surface of the nanoparticles. Because of the electron trap energy levels that are created when Mn^0 is doped onto the PBC surface, there are more holes available for the formation of (˙OH) radicals, and electron–hole pair recombination is reduced. When photogenerated holes react with water through an oxidation–reduction reaction, they produce hydroxyl radicals (˙OH), whereas electrons generated by light interact with molecular oxygen to make superoxide anions. The produced O^{2-} radical deteriorates water molecules to produce H_2O_2, which then combines with electrons to produce (˙OH) radicals. Less harmful byproducts are formed when these produced ROS species, namely O^{2-} and (˙OH), oxidatively react with the CPY pollutant.[55]

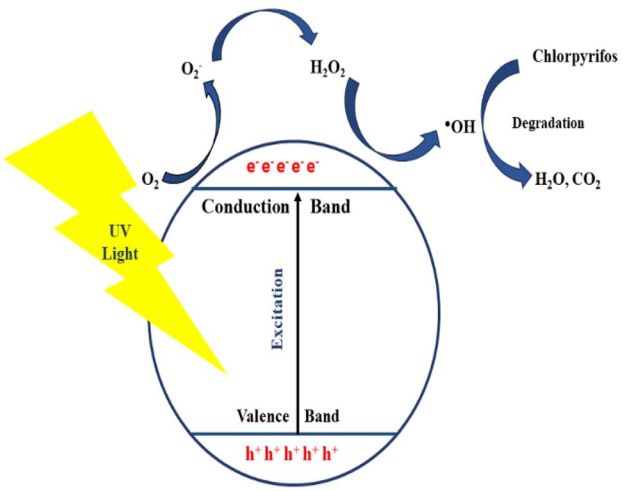

Fig. 8 Proposed photocatalytic degradation mechanism.

$$MnO + h\nu \rightarrow e_{cb}^- + h_{vb}^+ \quad (14)$$

$$e_{cb}^- + O_2 \rightarrow O_2^{\cdot -} \quad (15)$$

$$h_{vb}^+ + H_2O \rightarrow H^+ + {}^{\cdot}OH \quad (16)$$

$$h_{vb}^+ + {}^-OH \rightarrow {}^{\cdot}OH \quad (17)$$

$$O_2^{\cdot -} + H_2O \rightarrow H_2O_2 \quad (18)$$

$$H_2O_2 + e_{cb}^- \rightarrow 2OH^- \quad (19)$$

$$^{\cdot}OH + O_2^{\cdot -} + CPY \rightarrow \text{intermediate} + {}^{\cdot}OH \rightarrow DPs \quad (20)$$

The accelerated photocatalytic breakdown of CPY pesticide is therefore influenced by the presence of Mn^0 in biochar with respect to the charge exchange kinetics and separation of photogenerated e^-/h^+ pairs.

Hydrogen peroxide photolysis

Hydrogen peroxide photolysis by UV is one of the most effective advanced oxidation processes (AOPs). The UV/H_2O_2 system is based on the decomposition of hydrogen peroxide to hydroxyl radicals using ultraviolet irradiation with a wavelength below 280 nm.

Mechanism of hydrogen peroxide photolysis

The simplified mechanism of hydrogen peroxide is described as follows:

$$H_2O_2 + h\nu \rightarrow 2{}^{\cdot}OH \quad (21)$$

$$^{\cdot}OH + H_2O_2 \rightarrow HO_2^{\cdot} + H_2O \quad (22)$$

$$HO_2^{\cdot} + H_2O_2 \rightarrow {}^{\cdot}OH + H_2O + O_2 \quad (23)$$

$$2HO_2^{\cdot} \rightarrow O_2^{\cdot -} + H^+ \quad (24)$$

$$\tfrac{1}{2}O_2^{\cdot -} + H_2O \rightarrow H_2O_2 \quad (25)$$

$$\tfrac{1}{2}O_2^{\cdot -} + H_2O \rightarrow 2{}^{\cdot}OH \quad (26)$$

The homolytic cleavage of a hydrogen peroxide molecule, yielding two hydroxyl radicals, is described by eqn (21). A certain number of hydroxyl radicals react with the hydrogen peroxide molecules, yielding hydroperoxyl radicals (eqn (22)). Hydroperoxyl radicals then react with hydrogen peroxide, yielding the desired hydroxyl radicals (eqn (23)). Eqn (24) shows that superoxide radicals can be produced from hydroperoxide radicals. Superoxide can then be transformed into hydrogen peroxide or hydroxyl radicals in a water environment (eqn (25) and (26)). However, superoxide radicals appear in the reaction system, utilizing hydrogen peroxide decomposition to a much lower extent. Hydroxyl radicals produced by reactions (27) and

(28) can attack organic molecules and decompose them through various reaction intermediates into inorganic products, such as CO_2, H_2O, and relevant mineral acids.[90]

$$H_2O_2 + OH \rightarrow H_2O + HO_2^- \quad (27)$$

$$2HO_2^- + h\nu \rightarrow 2^{\bullet}OH + O_2 \quad (28)$$

Effect of $[H_2O_2]_0$ on the degradation of chlorpyrifos

The introduction of varying concentrations of hydrogen peroxide, 10, 15 and 20 mg L^{-1}, to nZVMn/PBC accelerated the breakdown of chlorpyrifos. Higher concentrations of $[H_2O_2]_0$ (from 10 to 20) enhanced the removal of chlorpyrifos from 70% to 95%. The combination of $[H_2O_2]_0$ with nZVMn/PBC generates hydroxyl radicals. Therefore, employing a higher concentration of $[H_2O_2]_0$ could accelerate the production rate of hydroxyl radicals, resulting in increased removal of chlorpyrifos.[91] However, an excessive quantity of hydrogen peroxide can have adverse effects on the degradation of chlorpyrifos. This is because the hydroxyl radical might combine with water to produce a hydroperoxyl radical ($HO_2^{\bullet}$) initiating an additional reaction that disrupts the removal processes of chlorpyrifos (eqn (29)–(33)).[92] At constant adsorbent dosage, nZVMn/PBC = 1000 mg L^{-1} and pH = 8.0, CPY elimination efficiency was promoted from 40% to 90% by increasing $[H_2O_2]_0$ concentration from 10 to 20 mg L^{-1} at a reaction interval of 60 minutes (Fig. S10).

$$H_2O_2 + {}^{\bullet}OH \rightarrow H_2O + HO_2^{\bullet} \quad k = 2.7 \times 10^7 \ M^{-1} \ S^{-1} \quad (29)$$

$$HO_2^{\bullet} + {}^{\bullet}OH \rightarrow H_2O + O_2 \quad k = 6.6 \times 10^9 \ M^{-1} \ S^{-1} \quad (30)$$

$$HO_2^{\bullet} + HO_2^{\bullet} \rightarrow H_2O_2 + O_2 \quad k = 8.3 \times 10^5 \ M^{-1} \ S^{-1} \quad (31)$$

$$HO_2^{\bullet} + H_2O_2 \rightarrow {}^{\bullet}OH + O_2 \quad k = 3.0 \ M^{-1} \ S^{-1} \quad (32)$$

$$^{\bullet}OH + {}^{\bullet}OH \rightarrow H_2O_2 \ k = 5.5 \times 10^7 \ M^{-1} \ S^{-1} \quad (33)$$

Proposed degradation mechanism of CPY

During the catalytic degradation of chlorpyrifos using the nZVMn@PBC composite, hydroxyl radicals ($^{\bullet}OH$) are generated mainly through redox reactions between Mn species and reactive oxygen species. Mn(II)/Mn(III)/Mn(IV) redox cycling facilitates electron transfer from zero-valent manganese (Mn^0) and carbon sites to dissolved oxygen or H_2O_2, forming $^{\bullet}OH$ radicals.[93] Additionally, the plant biochar (PBC) surface enhances the adsorption of chlorpyrifos and oxygen, promoting localized electron transfer. These $^{\bullet}OH$ radicals act as powerful oxidizing agents, attacking and breaking down the C–P, C–O, and aromatic bonds in chlorpyrifos, leading to its mineralization into less toxic products.[94]

The degradation pathway of chlorpyrifos (CPY) was comprehensively established and is illustrated in Scheme 1. A total of six degradation products (DP1–DP6) were identified, along with two inorganic byproducts, namely HCl and $-OCH_3$. These products collectively confirm that the degradation of CPY proceeds through a hydroxyl radical ($^{\bullet}OH$)-dependent mechanism.[95] The structural features of CPY, particularly the chlorine atom attached to the aromatic ring containing the nitrogen group and the double bond between phosphorus and sulfur, were recognized as the most reactive sites vulnerable to $^{\bullet}OH$ attack.[71] In pathway I, the degradation is initiated when $^{\bullet}OH$ attacks the C–Cl bond, resulting in the release of a chloride ion and the formation of DP1. A subsequent $^{\bullet}OH$ attack on DP1 removes the $-OCH_3$ group, converting it into DP2. The cleavage of C–O bonds within the ring then generates DP3, which further transforms into DP4 through a series of oxidation reactions.[96] Eventually, DP4 undergoes cleavage of the P–O bond, leading to the formation of DP5. Pathway II follows a distinct route, where $^{\bullet}OH$ directly attacks the P–O bond of CPY, yielding DP6 as an intermediate.[37] Hydroxylation of DP6 and the concurrent elimination of chloride ions, coupled with dissociation of the C–Cl bond, ultimately regenerate DP5. The presence of inorganic products such as HCl and $-OCH_3$ further supports the proposed degradation mechanism, indicating extensive mineralization of CPY under nZVMn-catalyzed H_2O_2 treatment.[97] This comprehensive analysis not only elucidates the oxidative degradation mechanism of chlorpyrifos but also underscores the efficiency of hydroxyl-radical-mediated pathways in transforming toxic organophosphorus pesticides into less harmful intermediates, contributing significantly to environmental detoxification strategies.[71] The toxicities of the DPs are represented in Table 5.

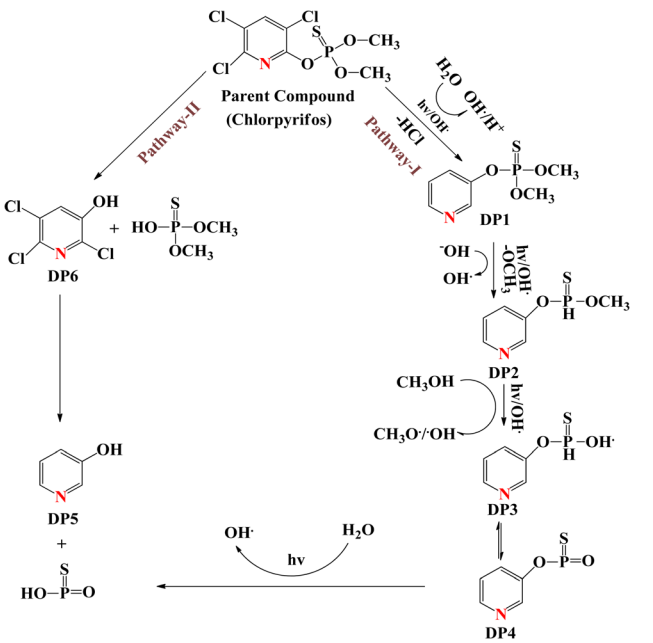

Scheme 1 Proposed degradation mechanism of CPY, catalyzed by H_2O_2 in the presence of nZVMn/biochar composite.

Table 5 Ecotoxicities of byproducts of chlorpyrifos[a]

DPA	Fish (LC_{50})	Daphnoid (LC_{50})	Green algae (EC_{50})	Fish (ChV)	Daphnoid (ChV)	Green algae (ChV)
PC (parent compound)	0.025	0.000958	0.995	0.028	7.4×10^{-5}	0.768
Baseline toxicity	3.264	2.256	3.783	0.482	0.388	1.534
DP1	3.555	0.010	21.340	1.500	0.000171	9.350
Baseline toxicity	306.686	178.047	114.809	29.148	15.521	28.515
DP2	6.314	0.017	39.745	3.432	0.000194	15.350
Baseline toxicity	793.768	419.005	231.005	71.202	33.371	51.440
DP3	45.602	0.092	326.691	49.424	0.00041	89.453
Baseline toxicity	15 996.2	7388.5	2343.9	1225.6	405.632	387.59
DP4	1465.78	4239.2	2941.2	210.7	7038.78	276.92
DP5	83.4876	16.645	83.762	7.359	3.171	39.814
Baseline toxicity	529.857	276.209	144.497	46.825	21.234	31.282
DP6	5.987	2.786	11.619	8.691	8.529	5.389
Baseline toxicity	28.282	12.639	13.833	2.213	1.597	4.457

[a] Acute toxicities following the EUP are $LC_{50} > 100$ or $EC_{50} > 100$ (harmless), $10 < LC_{50} < 100$ or $10 < EC_{50} < 100$ (harmful), $1 < LC_{50} <$ or $1 < EC_{50} < 10$ (toxic), $ChV < LC_{50} < EC_{50} < 5$ (less toxic), and $LC_{50} < 1$ or $EC_{50} < 1$ (very toxic); while chronic toxicities as listed in Chinese hazard evaluation criteria for new chemical substances (HJ/TI54-2004) are ChV > 10 (harmless), 1 < ChV < 10 (harmful), 0.1 < ChV < 10 (toxic) and ChV < 0.1 (very toxic).

Conclusion

In this study, the chemical reduction approach successfully produced nano-zero-valent manganese-doped plant biochar, which performed better in the removal of CPV from agricultural residues. It was discovered that Mn doping scavenges e_{cb}^-, freeing h_{vb}^+ for the reaction to produce $^{\bullet}OH$. Additionally, Mn doping rendered MnO more recyclable, and in contrast to MnO_2, nano-zero-valent manganese-doped plant biochar showed greater CPY degradation even after six treatment cycles. When peroxides, H_2O_2, and nZVMn/PBC were used under UV irradiation, reactive radicals were generated and CPY degradation was enhanced. Radical scavengers confirmed that reactive radicals were formed during peroxide stimulation. High quantities of H_2O_2 were found to accelerate CPY degradation because they more effectively inhibited coupling of e_{cb}^- and h_{vb}^+ and increased the rate at which $^{\bullet}OH$ was produced. In addition, the effects of various $[CPY]_0$ and initial pH on CPY degradation *via* UV-light-mediated nZVMn/PBC-catalyzed H_2O_2-based mechanisms were evaluated. The ecotoxicities of CPY and its transformation products (TPs) were evaluated using the ECOAR model, which revealed that the final products were non-toxic, indicating that the treatment technology is environmentally benign for CPY degradation.

Conflicts of interest

No conflicts of interest were found.

Data availability

The data supporting the findings of this study are available from the corresponding author upon reasonable request.

Supplementary information is available. See DOI: **https://doi.org/10.1039/d5ra06773a**.

Acknowledgements

The authors acknowledge the financial support through the Ongoing Research Funding Program – Research Chairs (ORF-RC-2025-0200), King Saud University, Riyadh, Saudi Arabia.

References

1 M. C. Vagi and A. S. Petsas, Recent advances on the removal of priority organochlorine and organophosphorus biorecalcitrant pesticides defined by Directive 2013/39/EU from environmental matrices by using advanced oxidation processes: An overview (2007–2018), *J. Environ. Chem. Eng.*, 2020, **8**(1), 102940.
2 Y. Abubakar, *et al.*, Pesticides, history, and classification, in *Natural Remedies for Pest, Disease and Weed Control*, Elsevier, 2020, pp. 29–42.
3 G. S. Kamble and Y.-C. Ling, Solvothermal synthesis of facet-dependent BiVO4 photocatalyst with enhanced visible-light-driven photocatalytic degradation of organic pollutant: assessment of toxicity by zebrafish embryo, *Sci. Rep.*, 2020, **10**(1), 12993.
4 H. U. ur Rahman, *et al.*, A comprehensive review on chlorpyrifos toxicity with special reference to endocrine disruption: Evidence of mechanisms, exposures and mitigation strategies, *Sci. Total Environ.*, 2021, **755**, 142649.
5 P. D. Sarvalkar, *et al.*, Bio-mimetic synthesis of catalytically active nano-silver using Bos taurus (A-2) urine, *Sci. Rep.*, 2021, **11**(1), 16934.
6 G. Echeverri-Jaramillo, *et al.*, Acute toxicity of chlorpyrifos and its metabolite 3, 5, 6-trichloro-2-pyridinol alone and in combination using a battery of bioassays, *Environ. Sci. Pollut. Res.*, 2020, **27**, 32770–32778.
7 P. D. Sanadi, *et al.*, Controllable synthesis of semiconducting anatase TiO2 nanostructures for visible light driven photocatalytic degradation of crystal violet and methylene blue dye, *Spectrochim. Acta, Part A*, 2025, 126404.

8 J. Perry, *et al.*, Organophosphate exposure and the chronic effects on farmers: a narrative review, *Rural Remote Health*, 2020, **20**(1), 206–222.
9 R. C. Ghaware, *et al.*, Degradation of organic Pollutant by Using of BiVO4–NiFe2O4 Heterostructure Photocatalyst under Visible Light Irradiation: Assessment of Detoxicity Study Using Cirrhinus mrigala, *Langmuir*, 2024, **40**(28), 14426–14439.
10 M. Bootharaju and T. Pradeep, Understanding the degradation pathway of the pesticide, chlorpyrifos by noble metal nanoparticles, *Langmuir*, 2012, **28**(5), 2671–2679.
11 D. Sud, *et al.*, Toxicity, natural and induced degradation of chlorpyrifos, *J. Chil. Chem. Soc.*, 2020, **65**(2), 4807–4816.
12 S. Sheikhi, R. Dehghanzadeh and H. Aslani, Advanced oxidation processes for chlorpyrifos removal from aqueous solution: a systematic review, *J. Environ. Health Sci. Eng.*, 2021, **19**(1), 1249–1262.
13 A. Mosa, A. El-Ghamry and M. Tolba, Biochar-supported natural zeolite composite for recovery and reuse of aqueous phosphate and humate: batch sorption–desorption and bioassay investigations, *Environ. Technol. Innovation*, 2020, **19**, 100807.
14 Y. Choi, *et al.*, Rank-ordered analysis of consumer preferences for the attributes of a value-added biofuel co-product, *Sustainability*, 2020, **12**(6), 2363.
15 F. Yang, *et al.*, Fabrication and characterization of hydrophilic corn stalk biochar-supported nanoscale zero-valent iron composites for efficient metal removal, *Bioresour. Technol.*, 2018, **265**, 490–497.
16 J. Iqbal, *et al.*, Nano-zerovalent manganese/biochar composite for the adsorptive and oxidative removal of Congo-red dye from aqueous solutions, *J. Hazard. Mater.*, 2021, **403**, 123854.
17 Z. Li, *et al.*, Biochar-supported nanoscale zero-valent iron as an efficient catalyst for organic degradation in groundwater, *J. Hazard. Mater.*, 2020, **383**, 121240.
18 M. B. Shakoor, *et al.*, A review of biochar-based sorbents for separation of heavy metals from water, *Int. J. Phytorem.*, 2020, **22**(2), 111–126.
19 X. Zhang, *et al.*, Enhanced H2O2 activation and sulfamethoxazole degradation by Fe-impregnated biochar, *Chem. Eng. J.*, 2020, **385**, 123921.
20 Z. Wan, *et al.*, A sustainable biochar catalyst synergized with copper heteroatoms and CO 2 for singlet oxygenation and electron transfer routes, *Green Chem.*, 2019, **21**(17), 4800–4814.
21 Y. Sun, *et al.*, Multifunctional iron-biochar composites for the removal of potentially toxic elements, inherent cations, and hetero-chloride from hydraulic fracturing wastewater, *Environ. Int.*, 2019, **124**, 521–532.
22 N. S. Shah, *et al.*, Hydroxyl and sulfate radical mediated degradation of ciprofloxacin using nano zerovalent manganese catalyzed S2O82−, *Chem. Eng. J.*, 2019, **356**, 199–209.
23 B. Murtaza, *et al.*, Synergistic effects of bismuth coupling on the reactivity and reusability of zerovalent iron nanoparticles for the removal of cadmium from aqueous solution, *Sci. Total Environ.*, 2019, **669**, 333–341.
24 J. Iqbal, *et al.*, Synthesis of nitrogen-doped Ceria nanoparticles in deep eutectic solvent for the degradation of sulfamethaxazole under solar irradiation and additional antibacterial activities, *Chem. Eng. J.*, 2020, **394**, 124869.
25 T. E. Samsam, D. L. Hunter and P. J. Bushnell, Effects of chronic dietary and repeated acute exposure to chlorpyrifos on learning and sustained attention in rats, *Toxicol. Sci.*, 2005, **87**(2), 460–468.
26 A. M. Betancourt, S. C. Burgess and R. L. Carr, Effect of developmental exposure to chlorpyrifos on the expression of neurotrophin growth factors and cell-specific markers in neonatal rat brain, *Toxicol. Sci.*, 2006, **92**(2), 500–506.
27 M. H. Silva, Effects of low-dose chlorpyrifos on neurobehavior and potential mechanisms: A review of studies in rodents, zebrafish, and Caenorhabditis elegans, *Birth Defects Res.*, 2020, **112**(6), 445–479.
28 J. G. Silva, *et al.*, Chlorpyrifos induces anxiety-like behavior in offspring rats exposed during pregnancy, *Neurosci. Lett.*, 2017, **641**, 94–100.
29 M. Muller, *et al.*, Neurologic dysfunction and genotoxicity induced by low levels of chlorpyrifos, *Neurotoxicology*, 2014, **45**, 22–30.
30 Y. Liang, *et al.*, Organophosphorus pesticide chlorpyrifos intake promotes obesity and insulin resistance through impacting gut and gut microbiota, *Microbiome*, 2019, **7**, 1–15.
31 I. Lee, *et al.*, Developmental neurotoxic effects of two pesticides: Behavior and biomolecular studies on chlorpyrifos and carbaryl, *Toxicol. Appl. Pharmacol.*, 2015, **288**(3), 429–438.
32 EFSA Panel on Plant Protection Products and their Residues (PPR), *et al.*, Investigation into experimental toxicological properties of plant protection products having a potential link to Parkinson's disease and childhood leukaemia, *EFSA J.*, 2017, **15**(3), 4691, DOI: 10.2903/j.efsa.2017.4691.
33 N. A. Baba, *et al.*, Toxic effects of fluoride and chlorpyrifos on antioxidant parameters in rats: protective effects of vitamins C and E, *Fluoride*, 2013, **46**(2), 73–79.
34 B. Wang, *et al.*, Preparation of biochar by simultaneous carbonization, magnetization and activation for norfloxacin removal in water, *Bioresour. Technol.*, 2017, **233**, 159–165.
35 X. Pan, *et al.*, Preparation of biochar and biochar composites and their application in a Fenton-like process for wastewater decontamination: A review, *Sci. Total Environ.*, 2021, **754**, 142104.
36 A. O. Dada, F. Adekola and E. Odebunmi, A novel zerovalent manganese for removal of copper ions: synthesis, characterization and adsorption studies, *Appl. Water Sci.*, 2017, **7**, 1409–1427.
37 M. Zahid, *et al.*, Photocatalytic Degradation of Norfloxacin Using Biochar Supported nZVMn/TiO_2 Nanocomposite: Synthesis, Characterization, and Performance Evaluation, *Surf. Interfaces*, 2025, 107034.

38 M. Imran, *et al.*, Potential of siltstone and its composites with biochar and magnetite nanoparticles for the removal of cadmium from contaminated aqueous solutions: batch and column scale studies, *Environ. Pollut.*, 2020, **259**, 113938.
39 M. Imran, *et al.*, Effect of biochar modified with magnetite nanoparticles and HNO3 for efficient removal of Cr (VI) from contaminated water: a batch and column scale study, *Environ. Pollut.*, 2020, **261**, 114231.
40 M. Anusuya, *et al.*, Green-synthesized flattened rice-shaped CuO and metal doped CuO nanoparticles using Bauhinia racemosa Lam. leaves extract and their photocatalytic and biological applications, *Inorg. Chem. Commun.*, 2024, **162**, 112289.
41 A. Belcaid, *et al.*, New insights on manganese dioxide nanoparticles loaded on cellulose-based biochar of cassava peel for the adsorption of three cationic dyes from wastewater, *Int. J. Biol. Macromol.*, 2023, **241**, 124534.
42 J. Iqbal, *et al.*, Efficient removal of norfloxacin using nano zerovalent cerium composite biochar-catalyzed peroxydisulfate, *J. Cleaner Prod.*, 2022, **377**, 134405.
43 H. Li, *et al.*, Mn2O3 as an electron shuttle between peroxymonosulfate and organic pollutants: the dominant role of surface reactive Mn (IV) species, *Environ. Sci. Technol.*, 2022, **56**(7), 4498–4506.
44 Z. Shi, *et al.*, Thallium removal from wastewater using sulfidized zero-valent manganese: Effects of sulfidation method and liquid nitrogen pretreatment, *Chemosphere*, 2023, **318**, 137971.
45 V. T. Trinh, *et al.*, Phosphate adsorption by silver nanoparticles-loaded activated carbon derived from tea residue, *Sci. Rep.*, 2020, **10**(1), 3634.
46 A. P. Panda, *et al.*, Core–shell structured zero-valent manganese (ZVM): a novel nanoadsorbent for efficient removal of As (iii) and As (v) from drinking water, *J. Mater. Chem. A*, 2019, **7**(16), 9933–9947.
47 M. Bellaj, *et al.*, Cationic and anionic dyes adsorption from wastewater by clay-chitosan composite: An integrated experimental and modeling study, *Chem. Eng. Sci.*, 2024, **285**, 119615.
48 J. D. Clogston and A. K. Patri, Zeta potential measurement, *Characterization of Nanoparticles Intended for Drug Delivery*, 2011, pp. 63–70.
49 R. Upadhyay, *et al.*, Band-gap tuning in Mn-doped Er2Ti2O7: insight from the experimental and theoretical approach, *J. Alloys Compd.*, 2024, **997**, 174767.
50 S. Mukherjee, *et al.*, Structure and electronic effects from Mn and Nb Co-doping for low band gap BaTiO3 ferroelectrics, *J. Phys. Chem. C*, 2021, **125**(27), 14910–14923.
51 M. I. Kholil and M. T. H. Bhuiyan, Effects of Cr-and Mn-alloying on the band gap tuning, and optical and electronic properties of lead-free CsSnBr 3 perovskites for optoelectronic applications, *RSC Adv.*, 2020, **10**(71), 43660–43669.
52 M. Fakharpour and M. H. K. Tafti, The energy band gap of the manganese oxide pyramidal nanostructures, *J. Mod. Opt.*, 2022, **69**(16), 911–916.
53 S. G. Muhamad, Kinetic studies of catalytic photodegradation of chlorpyrifos insecticide in various natural waters, *Arabian J. Chem.*, 2010, **3**(2), 127–133.
54 H. Khan, *et al.*, Impact of five insecticides on chickpea (Cicer arietinum L.) nodulation, yield and nitrogen fixing rhizospheric bacteria, *Soil Environ.*, 2009, **28**(1), 56–59.
55 N. S. Shah, *et al.*, Enhanced solar light photocatalytic performance of Fe-ZnO in the presence of H2O2, S2O82−, and HSO5− for degradation of chlorpyrifos from agricultural wastes: toxicities investigation, *Chemosphere*, 2022, **287**, 132331.
56 Y. Su, *et al.*, Acid Orange II degradation through a heterogeneous Fenton-like reaction using Fe–TiO 2 nanotube arrays as a photocatalyst, *J. Mater. Chem. A*, 2015, **3**(16), 8537–8544.
57 X. Shang, *et al.*, Efficient degradation of chlorpyrifos and intermediate in soil by a novel microwave induced advanced oxidation process: A two-stage reaction, *J. Hazard. Mater.*, 2024, **464**, 133001.
58 K. Balasubramani, N. Sivarajasekar and M. Naushad, Effective adsorption of antidiabetic pharmaceutical (metformin) from aqueous medium using graphene oxide nanoparticles: Equilibrium and statistical modelling, *J. Mol. Liq.*, 2020, **301**, 112426.
59 G. Sharma and M. Naushad, Adsorptive removal of noxious cadmium ions from aqueous medium using activated carbon/zirconium oxide composite: Isotherm and kinetic modelling, *J. Mol. Liq.*, 2020, **310**, 113025.
60 J. Iqbal, *et al.*, Synergistic effects of activated carbon and nano-zerovalent copper on the performance of hydroxyapatite-alginate beads for the removal of As3+ from aqueous solution, *J. Cleaner Prod.*, 2019, **235**, 875–886.
61 P. Nautiyal, K. Subramanian and M. Dastidar, Adsorptive removal of dye using biochar derived from residual algae after in-situ transesterification: alternate use of waste of biodiesel industry, *J. Environ. Manage.*, 2016, **182**, 187–197.
62 K. Aziz, *et al.*, Reduced and modified graphene oxide with Ag/V2O5 as a ternary composite visible light photocatalyst against dyes and pesticides, *Environ. Res.*, 2024, **247**, 118256.
63 P. Saharan, *et al.*, A comprehensive review on the metal-based green valorized nanocomposite for the remediation of emerging colored organic waste, *Environ. Sci. Pollut. Res.*, 2023, **30**(16), 45677–45700.
64 D. N. Ahmed, *et al.*, Waste foundry sand/MgFe-layered double hydroxides composite material for efficient removal of Congo red dye from aqueous solution, *Sci. Rep.*, 2020, **10**(1), 2042.
65 A. Hassani, *et al.*, Sonocatalytic degradation of ciprofloxacin using synthesized TiO2 nanoparticles on montmorillonite, *Ultrason. Sonochem.*, 2017, **35**, 251–262.
66 J. Iqbal, *et al.*, Deep eutectic solvent-mediated synthesis of ceria nanoparticles with the enhanced yield for photocatalytic degradation of flumequine under UV-C, *J. Water Proc. Eng.*, 2020, **33**, 101012.
67 C. M. Kgoetlana, S. P. Malinga and L. N. Dlamini, Photocatalytic degradation of chlorpyrifos with Mn-WO3/SnS2 heterostructure, *Catalysts*, 2020, **10**(6), 699.

68 J. Hou, *et al.*, Enhanced anaerobic biological treatment of chlorpyrifos in farmland drainage with zero valent iron, *Chem. Eng. J.*, 2018, **336**, 352–360.
69 H. Tang, *et al.*, Insights into enhanced removal of U (VI) by melamine sponge supported sulfurized nanoscale zero-valent iron, *J. Cleaner Prod.*, 2021, **329**, 129662.
70 S. B. Hammouda, *et al.*, Degradation and mineralization of phenol in aqueous medium by heterogeneous monopersulfate activation on nanostructured cobalt based-perovskite catalysts ACoO3 (A= La, Ba, Sr and Ce): characterization, kinetics and mechanism study, *Appl. Catal., B*, 2017, **215**, 60–73.
71 N. S. Shah, *et al.*, Nano zerovalent zinc catalyzed peroxymonosulfate based advanced oxidation technologies for treatment of chlorpyrifos in aqueous solution: a semi-pilot scale study, *J. Cleaner Prod.*, 2020, **246**, 119032.
72 M. Tharmavaram, *et al.*, Chitosan functionalized Halloysite Nanotubes as a receptive surface for laccase and copper to perform degradation of chlorpyrifos in aqueous environment, *Int. J. Biol. Macromol.*, 2021, **191**, 1046–1055.
73 T. Anirudhan, *et al.*, Highly efficient photocatalytic degradation of chlorpyrifos in aqueous solutions by nano hydroxyapatite modified CFGO/ZnO nanorod composite, *J. Photochem. Photobiol., A*, 2021, **418**, 113333.
74 G. Murtaza, *et al.*, A review of mechanism and adsorption capacities of biochar-based engineered composites for removing aquatic pollutants from contaminated water, *Front. Environ. Sci.*, 2022, **10**, 1035865.
75 E. Issaka, *et al.*, Biochar-based composites for remediation of polluted wastewater and soil environments: Challenges and prospects, *Chemosphere*, 2022, **297**, 134163.
76 X. Yuan, *et al.*, Recent advancements and challenges in emerging applications of biochar-based catalysts, *Biotechnol. Adv.*, 2023, **67**, 108181.
77 X. Zhang, *et al.*, Complexation and degradation of tetracycline by activation of molecular oxygen with biochar-supported nano-zero-valent copper composite, *Environ. Sci. Pollut. Res.*, 2023, **30**(12), 34827–34839.
78 R. Nekooie, T. Shamspur and A. Mostafavi, Novel CuO/TiO2/PANI nanocomposite: Preparation and photocatalytic investigation for chlorpyrifos degradation in water under visible light irradiation, *J. Photochem. Photobiol., A*, 2021, **407**, 113038.
79 R. Mansourian, *et al.*, CeO2/TiO2/SiO2 nanocatalyst for the photocatalytic and sonophotocatalytic degradation of chlorpyrifos, *Can. J. Chem. Eng.*, 2022, **100**(3), 451–464.
80 M. A. Farrukh, *et al.*, Influence of pH and temperature on structural, optical and catalytical investigations of CeO2-SiO2 nanoparticles, *Silicon*, 2019, **11**(6), 2591–2598.
81 M. A. Farrukh, *et al.*, Photoluminescence emission behavior on the reduced band gap of Fe doping in CeO2-SiO2 nanocomposite and photophysical properties, *J. Saudi Chem. Soc.*, 2019, **23**(5), 561–575.
82 F. Soltani-nezhad, *et al.*, Photocatalytic degradation of imidacloprid using GO/Fe3O4/TiO2-NiO under visible radiation: Optimization by response level method, *Polyhedron*, 2019, **165**, 188–196.
83 M. Rashidimoghaddam, *et al.*, Constructing S-doped Ni–Co LDH intercalated with Fe 3 O 4 heterostructure photocatalysts for enhanced pesticide degradation, *New J. Chem.*, 2020, **44**(36), 15584–15592.
84 D. Pathania, *et al.*, Bio-synthesized Cu–ZnO hetro-nanostructure for catalytic degradation of organophosphate chlorpyrifos under solar illumination, *Chemosphere*, 2021, **277**, 130315.
85 M. Rani, J. Yadav and U. Shanker, Green synthesis of sunlight responsive zinc oxide coupled cadmium sulfide nanostructures for efficient photodegradation of pesticides, *J. Colloid Interface Sci.*, 2021, **601**, 689–703.
86 S. H. Khan, B. Pathak and M. Fulekar, Synthesis, characterization and photocatalytic degradation of chlorpyrifos by novel Fe: ZnO nanocomposite material, *Nanotechnol. Environ. Eng.*, 2018, **3**, 1–14.
87 M. K. Choudhary, *et al.*, Green biomimetic preparation of efficient Ag–ZnO heterojunctions with excellent photocatalytic performance under solar light irradiation: a novel biogenic-deposition-precipitation approach, *Nanoscale Adv.*, 2019, **1**(3), 1035–1044.
88 F. Liu, H. Tian and J. He, Adsorptive performance and catalytic activity of superparamagnetic Fe3O4@ nSiO2@ mSiO2 core–shell microspheres towards DDT, *J. Colloid Interface Sci.*, 2014, **419**, 68–72.
89 P. Vindhya and V. Kavitha, Leaf extract-mediated synthesis of Mn-doped CuO nanoparticles for antimicrobial, antioxidant and photocatalytic applications, *Chem. Pap.*, 2023, **77**(5), 2407–2424.
90 P. Krystynik, Advanced oxidation processes (aops)—utilization of hydroxyl radical and singlet oxygen, *React. Oxygen Species*, 2021.
91 J. A. Khan, *et al.*, Oxidative degradation of atrazine in aqueous solution by UV/H2O2/Fe2+, UV/S2O82-/Fe2+ and UV/HSO5-/Fe2+ processes: a comparative study, *Chem. Eng. J.*, 2013, **218**, 376–383.
92 A. G. d. Oliveira, *et al.*, Degradation of the pesticide chlorpyrifos in aqueous solutions with UV/H2O2: optimization and effect of interfering anions, *J. Adv. Oxid. Technol.*, 2014, **17**(1), 133–138.
93 C. Mattei, H. Wortham and E. Quivet, Heterogeneous degradation of pesticides by OH radicals in the atmosphere: influence of humidity and particle type on the kinetics, *Sci. Total Environ.*, 2019, **664**, 1084–1094.
94 Q. V. Vo, *et al.*, The reaction of acetamiprid with OH radicals in the environment: a theoretical study, *RSC Adv.*, 2025, **15**(24), 19236–19244.
95 S. Sun, K. Zhang and H. Zhang, Theoretical study on the degradation mechanism of carbamate pesticides with OH radicals, *Theor. Chem. Acc.*, 2015, **134**(3), 25.
96 K. L. Armbrust, Pesticide hydroxyl radical rate constants: measurements and estimates of their importance in aquatic environments, *Environ. Toxicol. Chem.*, 2000, **19**(9), 2175–2180.
97 M. Zahid, *et al.*, Biochar-derived photocatalysts for pharmaceutical waste removal, a sustainable approach to water purification, *Appl. Surf. Sci. Adv.*, 2025, **26**, 100721.